Spin-spiral state of a Mn monolayer on W(110) studied by soft x-ray absorption spectroscopy at variable temperature

J. Honolka[1,*] S. Krotzky,[2] M. Herzog,[3] T. Herden,[2] V. Sessi,[4] H. Ebert,[5] J. Minár,[6] K. von Bergmann[3] R. Wiesendanger[3] and O. Šipr[7,†]

[1]*FZU-Institute of Physics of the Czech Academy of Sciences, Na Slovance 2, CZ-182 21 Prague, Czech Republic*
[2]*Max Planck Institute for Solid State Research, Heisenbergstrasse 1, D-70569 Stuttgart, Germany*
[3]*Department of Physics, University of Hamburg, Jungiusstrasse 11A, D-20355 Hamburg, Germany*
[4]*European Synchrotron Radiation Facility (ESRF), 71 Avenue des Martyrs, F-38000 Grenoble, France*
[5]*Department of Chemistry, Ludwig-Maximilians-Universität München, Butenandtstrasse 11, D-81377 München, Germany*
[6]*New Technologies Research Centre, University of West Bohemia, Univerzitní 8, CZ-301 00 Pilsen, Czech Republic*
[7]*FZU-Institute of Physics of the Czech Academy of Sciences, Cukrovarnická 10, CZ-162 53 Prague, Czech Republic*

(Received 3 December 2020; accepted 4 May 2021; published 17 May 2021)

The noncollinear magnetic state of epitaxial Mn monolayers on tungsten (110) crystal surfaces is investigated by means of soft x-ray absorption spectroscopy to complement earlier spin-polarized scanning tunneling microscopy experiments. X-ray absorption spectra (XAS), x-ray linear dichroism (XLD) and field-induced x-ray magnetic circular dichroism (XMCD) Mn $L_{2,3}$-edge spectra were measured in the temperature range from 8 to 300 K and compared to results of fully relativistic *ab initio* calculations. We show that antiferromagnetic (AFM) helical and cycloidal spirals give rise to significantly different Mn $L_{2,3}$-edge XLD signals, enabling, thus, to distinguish between them. It follows from our results that the magnetic ground state of a Mn monolayer on W(110) is an AFM cycloidal spin spiral. Based on temperature-dependent XAS, XLD, and field-induced XMCD spectra we deduce that magnetic properties of the Mn monolayer on W(110) vary with temperature, but this variation lacks a clear indication of a phase transition in the investigated temperature range up to 300 K—even though a crossover exists around 170 K in the temperature dependence of XAS branching ratios and in XLD profiles.

DOI: 10.1103/PhysRevB.103.174419

I. INTRODUCTION

Noncollinear magnetic states have attracted a lot of attention lately. However, experimental investigations of noncollinear magnetism are difficult: Standard spatial-averaging techniques cannot be used because the average magnetization is zero. New techniques have to be sought. It was demonstrated that scanning tunneling microscopy (STM) with magnetic or nonmagnetic tips can provide valuable information about local magnetic order [1]. In particular, a Mn monolayer (ML) on W(110) [called Mn/W(110) hereafter] has become a playground for studying noncollinear magnetism. Ordered Mn monolayer stripes can be prepared on stepped W(110) single-crystal substrates by epitaxial step-flow growth [2]. First studies of the magnetic order of Mn/W(110) by spin-polarized STM experiments [3] as well as *ab initio* calculations [3,4] suggested a collinear antiferromagnetic (AFM) order. Later, field-dependent spin-polarized STM experiments with atomic resolution for a larger field of view revealed a periodic magnetic pattern along the $[1\bar{1}0]$ direction of W(110) with a wavelength λ of about 12 nm, indicating an AFM cycloidal or helical spin-spiral magnetic ground state [5]. Theoretical investigations accounting for the Dzyaloshinskii-Moriya interaction proposed that the ground state should be a left-handed AFM cycloidal spin spiral [5]. Later, additional field-dependent STM measurements provided further evidence in favor of this [6]. Recently the Mn/W(110) system was exploited as a substrate inducing noncollinear magnetism in adatoms [7–9].

The temperature dependence of the magnetic order of Mn/W(110) is especially interesting. Estimates of the Néel temperature T_N based on theoretical and experimental studies differ substantially: Atomistic simulations of the magnetic order with the input parameters taken from *ab initio* calculations yield T_N of about 510 K whereas STM studies exploiting the spin-orbit contrast suggest T_N to be about 240 K [10] with additional dependence of T_N on the structural width of Mn monolayer stripes along the [001] direction [11]. These results could be reconciled by considering different timescales probed by the experiment in connection with thermal depinning of the spin spirals. Neither theory nor STM experiment found any indication for an intermediate magnetic state between the cycloidal spin spiral (CSS) state and a paramagnetic state at higher temperatures.

Even though spin-polarized STM is a very powerful method, it may not provide the full picture. In particular, if a thermal depinning takes place for a spin-spiral state, it is possible that the spin spiral moves along its propagation direction, resulting in a phase shift. When this process is fast compared to the timescale of the measurement, i.e., the

*honolka@fzu.cz
†sipr@fzu.cz

settling time of the STM tip per pixel, only a time-averaged signal is obtained [10,12]. Regarding spatial information, typical surface imaging areas of STM are up to few hundreds of nanometers, which is a limitation when a large variety of Mn stripe geometries exists and good statistics is achieved only on larger areas. Employing a complementary technique which would provide instantaneous time snapshots for a representative part of the sample is, thus, desirable.

A suitable technique in this respect is x-ray absorption spectroscopy. It is chemically specific, so one knows that one gets a view on the electronic states from an atom of a given type and, at the same time, the inspected area is macroscopic (typically 0.1×0.3 mm^2). Dichroic techniques studying the change in the x-ray absorption spectrum (XAS) upon changing the polarization vectors of the incoming x rays and/or the direction of the magnetization proved to be powerful for studying ferromagnetic as well as antiferromagnetic order. For studying complicated noncollinear magnetic order, such as the one formed in Mn/W(110), XAS spectroscopy was used only scarcely [13–15]. However, dealing with its complexity is worthy because x-ray absorption spectroscopy can be viewed as a complementary technique to STM.

So far, x-ray magnetic linear dichroism (XMLD) techniques were mostly applied to collinear AFM bulk systems where there would be no dichroic signal without magnetic order—see, e.g., Refs. [16–18]. In such cases the orientation of x-ray polarization vectors with respect to the crystal affects the shape and intensity of the XMLD spectra [17,19], but the very reason for the effect is magnetic. When studying Mn/W(110), one encounters a different situation: There is also a strong structural component of the dichroism, stemming from the nonfourfold symmetry of the bcc (110) crystal surface. The magnetic order is an additional factor affecting the spectrum.

Our study focuses on measuring temperature-dependent XAS at the Mn $L_{2,3}$ edges and the respective XLD and field-induced x-ray magnetic circular dichroism (XMCD) for Mn/W(110) and on comparing these data to *ab initio* calculations. This enables us to assess to what extent the XLD technique can be applied to distinguish between various noncollinear magnetic configurations. In particular, we find that, for the particular case of Mn/W(110), the XLD technique is sensitive to the differences between cycloidal and helical spin spirals. Another important issue we explore is how the magnetic order of Mn/W(110) changes if the temperature increases from 8 K up to room temperature. Magnetic properties of Mn/W(110) vary with temperature, but there is no clear indication of a phase transition in the investigated range. Nevertheless, a crossover around 170 K is apparent in the temperature dependence of L_3- to L_2-XAS branching ratios and in XLD profiles (but not in XMCD); the exact nature of this crossover is not clear.

II. METHODS

A. Sample preparation

W(110) crystal preparation and Mn deposition were performed *in situ* in the UHV preparation chamber of the ID8 beamline at ESRF. W(110) single crystals were mounted on standard Omicron plates and cleaned in a standard two-step process described elsewhere [5]: The crystal was annealed at $T = 1200\,^{\circ}$C in an oxygen atmosphere, and the surface oxide formed during this process is, thereafter, removed by a short flash to $T = 1800\,^{\circ}$C. This cycle was repeated until STM and low-energy electron diffraction (LEED) showed well-ordered and clean surface properties.

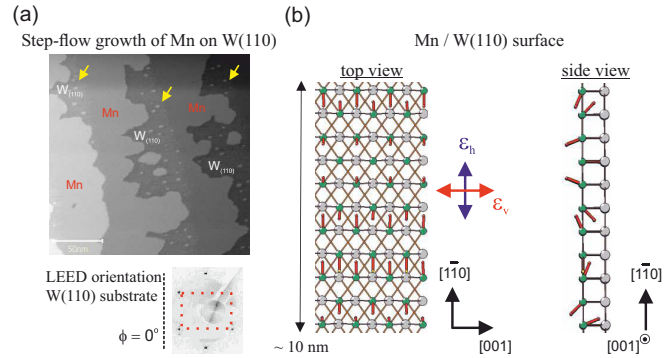

FIG. 1. (a) STM image of the Mn/W(110) surface with a Mn coverage of about 80% of a ML. Yellow arrows indicate W(110) step edges. The LEED image of the W(110) surface taken before Mn growth defines the azimuthal orientation $\phi = 0^{\circ}$ with respect to ϵ_h and ϵ_v incoming photon polarization vectors. (b) Schematic of the surface atomic configuration and respective orientation of ϵ_h and ϵ_v photon polarization vectors for $\phi = 0^{\circ}$. The small dark circles denote Mn atoms, the large light circles denote W atoms in the subsurface layer. Rods at Mn atoms indicate symbolically the directions of magnetic moments for an antiferromagnetic CSS.

Mn was evaporated from a crucible with deposition rates of approximately 0.1 ML/min (evaporator parameters: 1.9 A, 11.4 mA, 500 V, and 300 nA). The deposition rate was calibrated by STM. During deposition the W crystals were kept at about 200 °C, which leads to a step-flow growth of Mn monolayer stripes along W step edges as shown in Fig. 1(a). Coverages and morphology of the Mn monolayers were highly reproducible in STM when samples were reprepared from scratch using the same parameters. The homogeneity of the Mn coverages was verified by respective *in situ* XAS data—the Mn $L_{2,3}$-white line intensities differed by 4% at most. Further STM images of the W(110) substrate and Mn/W(110) sample are shown in Appendix A. After fresh preparation the samples were immediately transferred *in situ* to the XAS chamber at ID8.

In order to change the azimuthal orientation (see Sec. II B), the W(110) crystal was *ex situ* rotated on the Omicron sample holder and reentered into the UHV chambers. The *in situ* tungsten cleaning procedures described in Sec. II A were repeated, thereafter, followed by a fresh Mn monolayer preparation and respective STM characterization.

B. Measurement

XAS was measured at the Mn $L_{2,3}$-edges (x-ray energy 630–680 eV) at the ID8 beamline for temperatures varying from 8 to 300 K in the surface sensitive total electron yield (TEY) mode. The beamline is known for its high resolution in the detection of $L_{2,3}$-XAS signals for ultralow coverages down

to 1% of a monolayer. XLD was measured in a polar geometry ($\Theta = 0^\circ$) with horizontal ϵ_h and vertical ϵ_v x-ray polarization vectors (in the laboratory coordinates) of the Apple II undulator. A small magnetic field of $B = 100$ mT was applied during the XLD measurements to reduce the TEY noise.

The XLD spectra were recorded for two different azimuthal crystal orientations: (i) The $[1\bar{1}0]$ direction of the W crystal was parallel to the x-ray polarization vector ϵ_h [$\phi = 0 \pm 2^\circ$—as depicted in Fig. 1(b)], and (ii) the direction W$[1\bar{1}0]$ forms an angle $\phi = 48 \pm 2^\circ$ with ϵ_h. These azimuthal orientations were derived from *in situ* W(110) LEED patterns [as shown, e.g., at the bottom of Fig. 1(a)].

The field-induced XMCD spectra were measured for two incidence angles, namely, $\Theta = 0^\circ$ (polar incidence) and $\Theta = 70^\circ$ (grazing incidence with the plane of incidence defined by the W[110] and W$[1\bar{1}0]$ directions). During XMCD measurements an external magnetic field $B = \pm 5$ T is oriented parallel to the photon beam. The XMCD signal, thus, reflects the average Mn magnetizations induced by the external magnetic field along the respective photon beam directions.

Dichroism signals are defined as

$$\mathrm{XLD} = \mu(\epsilon_v) - \mu(\epsilon_h) \equiv \mu(\epsilon \parallel \mathrm{W}[001]) - \mu(\epsilon \parallel \mathrm{W}[1\bar{1}0]), \tag{1}$$

with $\mu(\epsilon)$ denoting the absorption coefficient for incoming photon polarization vector ϵ, and

$$\mathrm{XMCD} = \mu(\epsilon_+) - \mu(\epsilon_-). \tag{2}$$

The respective average nondichroic signals are defined as

$$\mathrm{XAS} = [\mu(\epsilon_h) + \mu(\epsilon_v)]/2 \tag{3}$$

for linearly polarized x rays and

$$\mathrm{XAS} = [\mu(\epsilon_+) + \mu(\epsilon_-)]/2 \tag{4}$$

for circularly polarized x rays. All XAS signals are routinely normalized to unity at the Mn preedge at 635 eV to compensate variations of the base TEY signal, e.g., due to different incident photon beam intensities.

As a quantitative measure of the average moment per Mn atom we will use the so-called XMCD asymmetry. It is defined as the ratio between the L_3-XMCD peak intensity and the respective L_3-XAS peak intensity,

$$\text{XMCD asymmetry} = \mathrm{XMCD}_{L_3}/\mathrm{XAS}_{L_3} \tag{5}$$

evaluated at the L_3 edge (at about 641 eV in our case).

To check the correct photon energy calibration, the signal of a reference MnO polycrystalline sample was monitored during all polarization-dependent measurements to verify the absence of XLD in the reference sample at all times (see Fig. 9 in Appendix B).

C. Calculations

Accompanying calculations were performed within the *ab initio* framework of spin-density functional theory, relying on the generalized gradient approximation using the Perdew, Burke, and Ernzerhof functional [20]. The electronic structure embodied in the underlying effective single-particle Dirac Hamiltonian was calculated in a fully relativistic mode using the spin-polarized Green's function multiple-scattering (KKR-GF) formalism [21] as implemented in the SPRKKR code [22].

The Mn/W(110) system was modeled by a slab consisting of six W layers and a Mn layer, embedded in vacuum (represented by three layers of empty sites above the Mn layer). The lattice constant of bcc W was set to $a_0 = 3.165$ Å, and the vertical distance between the Mn monolayer and the nearest W layer to 2.12 Å, in agreement with earlier *ab initio* calculations [2,4]. First, the electronic structure of the two-dimensional slab was calculated by means of the tight-binding KKR technique [23] to obtain self-consistent potentials. Afterwards, the spectra were evaluated by the real-space calculations, using a cluster of 10.40-Å radius containing 181 atoms (or 315 atoms if counting empty vacuum sites as well). We checked that increasing the cluster further does not lead to significant changes in the results. Raw theoretical spectra were broadened by Lorentzians with full widths at half maxima 0.70 eV (L_2 edge) and 0.35 eV (L_3 edge) to account for the finite core hole lifetime.

Spectra for spin spirals were evaluated as averages of spectra for two AFM configurations with perpendicular directions of the magnetization. In particular, spectra for AFM CSSs are evaluated by averaging spectra for AFM configurations with $\boldsymbol{M} \parallel \mathrm{W}[1\bar{1}0]$ and with $\boldsymbol{M} \parallel \mathrm{W}[110]$ whereas spectra for the AFM helical spin spiral are evaluated by averaging spectra for AFM configurations with $\boldsymbol{M} \parallel \mathrm{W}[001]$ and with $\boldsymbol{M} \parallel \mathrm{W}[1\bar{1}0]$. One can view this approach as taking the long-wavelength limit. We checked by explicit calculations that this approach is justified in our case (see Appendix C). Note that a similar representation of CSS with a collinear AFM configuration was employed recently for *ab initio* calculations of the magnetic exchange force between a STM tip and Mn atoms on W(110) [24]. Dealing with the long-wavelength limit means that we cannot, in principle, distinguish between the rotational senses of the cycloidal spirals (right or left handed).

The potential was without any shape approximation, i.e., a full potential mode was employed, relying on the representation of the atomic cells by means of the shape functions [25,26]. The core hole was included within the final-state approximation, i.e., the hole is relaxed and screened. Technically, this was achieved within the single-site impurity approach (see Ref. [27] for more details). Accounting for the full potential and the core hole does not lead to significant changes in XAS, but it is important for the dichroic spectra. The influence of the core hole is illustrated in Appendix D.

The angular momentum cutoff used for calculating the spectra was $\ell_{\max} = 3$. A lower cutoff of $\ell_{\max} = 2$ would be sufficient for XAS and XMCD, but to get reliable results for XLD, $\ell_{\max} = 3$ was needed. The need for $\ell_{\max}$ larger than what is common for such systems is probably associated with the fact that the Mn $L_{2,3}$-edge XLD signal is quite small and, therefore, a high accuracy is needed. If an even larger cutoff of $\ell_{\max} = 4$ is used, no significant changes with respect to the $\ell_{\max} = 3$ case occur.

When interpreting experimental spectra recorded at elevated temperatures one has to consider a situation when there are local magnetic moments at Mn atoms but without any order—we call such a system paramagnetic. We model this by a disordered local moment (DLM) state: A Mn site is occupied with the same probability by an atom with spin

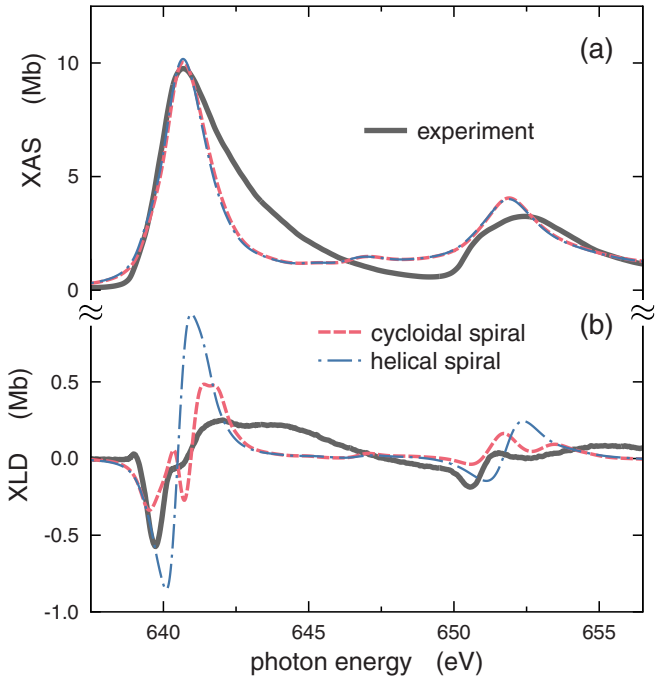

FIG. 2. (a) Experimental XAS and (b) XLD spectrum recorded at 8 K compared to spectra calculated for AFM cycloidal spin spiral and AFM helical spin spiral states.

up and by an atom with spin down [28]. Technically, this is achieved via the coherent potential approximation, which can be conveniently implemented within the KKR-GF formalism. To simulate the disorder also concerning the *directions* of the magnetic moments, additional averaging of spectra calculated for the magnetization oriented along three perpendicular directions ($\boldsymbol{M} \parallel$ W[001], $\boldsymbol{M} \parallel$ W[1$\bar{1}$0], $\boldsymbol{M} \parallel$ W[110]) is performed. Finally, we dealt also with nonmagnetic Mn; in such a case the potentials for the spin-up and spin-down electrons are identical and the local magnetic moments are zero.

III. RESULTS

A. Magnetic ground state: cycloidal versus helical spirals

Experimental Mn $L_{2,3}$-edge XAS and XLD spectra of Mn/W(110) recorded at $T = 8$ K in normal incidence geometry ($\Theta = 0^\circ$) for azimuthal orientation of the tungsten crystal $\phi = 0^\circ$ are shown in Fig. 2 (solid gray lines). The XAS spectral shape looks broad, typical for Mn atoms in a metallic state [29]. At the L_2 edge a faint shoulder is visible at around 651 eV. The fact that the spectrum resembles spectra of Mn in a metallic state suggests that atomiclike multiplet effects will be less significant. This is even more probable for XLD where the extended aspects of electronic states are important. Using an *ab initio* theoretical scheme, which accounts for the delocalized nature of electron states, thus, seems plausible.

We put the experimental XLD to test by verifying that it conforms the fundamental C_{2v} symmetry of the system. To achieve this, we compare the XLD signals measured at two different azimuthal crystal orientations $\phi = 0^\circ$ and $\phi = 48^\circ$. The signal recorded at $\phi = 48^\circ$ scales very accurately with the signal recorded at $\phi = 0^\circ$ with the scaling factor $\cos(2\phi) = -0.105$ (Fig. 10 in Appendix B). The measured signal, thus, indeed corresponds to the linear dichroism effect. Let us note that the XLD signal is quite small, just a few percent of the average XAS signal as evident from the units on the vertical axis of Fig. 2. Polarization-resolved spectra $\mu(\epsilon_h)$ and $\mu(\epsilon_v)$ defined in Eqs. (1) and (3) would, thus, be visually hardly distinguishable from the polarization-averaged spectrum.

The theoretical spectra shown in Fig. 2 were calculated assuming a CSS and a helical spin spiral configuration. The spectra were aligned in energy so that the theoretical L_3-edge white line maximum coincides with experiment. On the other hand, the vertical scaling of the spectra was performed by scaling the experimental XAS spectrum so that it matches the theoretical spectrum at the high-energy tail (because the theory provides absolute units for the XAS cross section). XLD spectra were scaled by the same factor as XAS spectra.

Theoretical XAS spectra (practically identical for both magnetic configurations) reproduce the gross features of the experiment but fail to reproduce the asymmetric shape of the white lines. This seems to be a general feature of *ab initio* calculations of $L_{2,3}$-edge spectra of transition metals and probably is associated with deficiencies of the final-state approximation in describing the core-hole effect in metals [30]. The shoulder at 651 eV observed in experiment probably stems from multiplet effects: It does not appear in Mn $L_{2,3}$-edge XAS of elemental Mn, but it is present for Mn-containing semiconductors and insulators [29,31] and for Mn monolayers on Ag(001) [32] and on Fe(001) [14]. If the coverage is increased, the shoulder at 651 eV gradually disappears [32]. So we can interpret these features in Fig. 2 as indications that the electron states of Mn have a partially local atomiclike character in our system and that some aspects of theirs cannot be fully accounted for within common implementations of the SDFT. The features are, nevertheless, small, meaning that the metallic character prevails.

There is no clear experimental counterpart to the small peak appearing in the calculated XAS spectrum at 647 eV [Fig. 2(a)]. This resembles the situation for transition-metal Fe and Co [30,33]. As discussed in Ref. [33], it is probably related to a van Hove singularity.

Concerning the XLD, one can see that cycloidal and helical spin spirals give rise to significantly different signals [Fig. 2(b)]. The helical spin spiral generates a simple derivativelike (plus/minus) structure both at the L_3 and L_2 edges, whereas the CSS shows a more complex XLD line shape. Theoretical data for a CSS reproduce the main features of the experimental data. Nevertheless, differences in details remain, especially further away from the edge. This may be partially linked to the presence of minor multiplet effects in the spectra. Another factor to consider is the possible presence of a second Mn layer in minor areas of the sample: Although the Mn coverage is below one monolayer and no double-layer Mn islands are observed in the STM image of Fig. 1(a), we cannot exclude seeds of a second Mn layer in other parts of the probed surface area. However, we checked a reference sample with coverage as low as 30% and the spectral shape of the XLD is very similar, suggesting that we really deal with essentially a monolayer system.

The theoretical XLD spectrum for a helical spiral fits the experiment much worse than the theoretical XLD spectrum

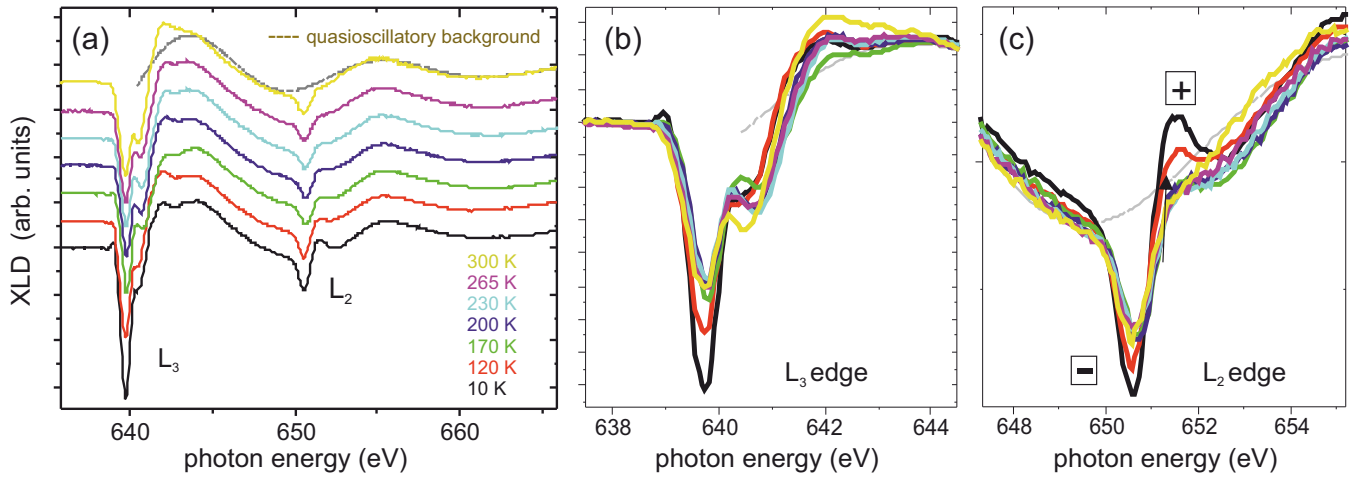

FIG. 3. (a) Temperature dependence of the XLD signal. The data are shown with a vertical offset for better visibility. The dashed curve on top of the $T = 300$-K curve represents a fitted temperature-independent background. (b) Detailed view of temperature-dependent XLD at the L_3 edge without the vertical offset. (c) As panel (b) but for the L_2 edge. The minus/plus signs indicate features where the temperature dependence of the XLD is most pronounced.

for a cycloidal spiral—in particular, as concerns the characteristic wiggle at 640.5 eV. So we conclude that soft x-ray absorption spectroscopy confirms that the magnetic ground state of Mn/W(110) is an AFM cycloidal spin spiral.

B. Temperature-dependent XLD

Figure 3 summarizes the temperature dependence of XLD signals from $T = 8$ to 300 K for the $\phi = 0°$ azimuthal orientation of the W crystal. An overall view is presented in Fig. 3(a) (with an *ad hoc* vertical offset between the curves), detailed views on the XLD at the L_3 and L_2 edges are shown in Figs. 3(b) and 3(c) (without offsets). The data can be decomposed into a temperature-independent broad quasioscillatory background [the dashed curve in Fig. 3(a)] and temperature-dependent features at the L_3 and L_2 edges.

The XLD profile changes with temperature. A closer inspection of the respective data in Fig. 3 reveals that most of the change occurs between 8 and 170 K. Minor changes occur between 170 and 300 K, especially at the L_3 edge. As a whole, the changes are gradual without any abrupt jumps which would signal phase transitions.

To learn how the decay of the magnetic order could possibly influence the spectra, we calculated Mn $L_{2,3}$-edge XAS and XLD assuming that: (i) Mn is nonmagnetic and (ii) that Mn is paramagnetic (by averaging DLM spectra for three perpendicular directions of the magnetization, see Sec. II C). The XAS spectra are shown in Fig. 4(a) together with theoretical spectrum for a CSS and with experimental spectra recorded for $T = 8$ and 300 K. The experimental spectra practically do not change if the temperature is increased. Likewise, we see only small changes in the theoretical spectra when going from a CSS to the paramagnetic case. However, the Mn $L_{2,3}$-edge XAS for nonmagnetic Mn/W(110) differs quite a lot regarding the intensity of the L_3- and L_2-white lines (even though the spectra are similar in the high-energy tail region, for $E \gtrsim 655$ eV). This is in accordance with the changes in the density of states (DOS): There is a big increase in the DOS just above E_F if the system is made nonmagnetic (see Fig. 13 in Appendix E). The fact that there is no big difference between experimental XAS for $T = 8$ and 300 K can, thus, be seen as a proof that there are local magnetic moments present at Mn atoms up to room temperature. To a certain degree this is reminiscent of the situation for Fe and Co where the local

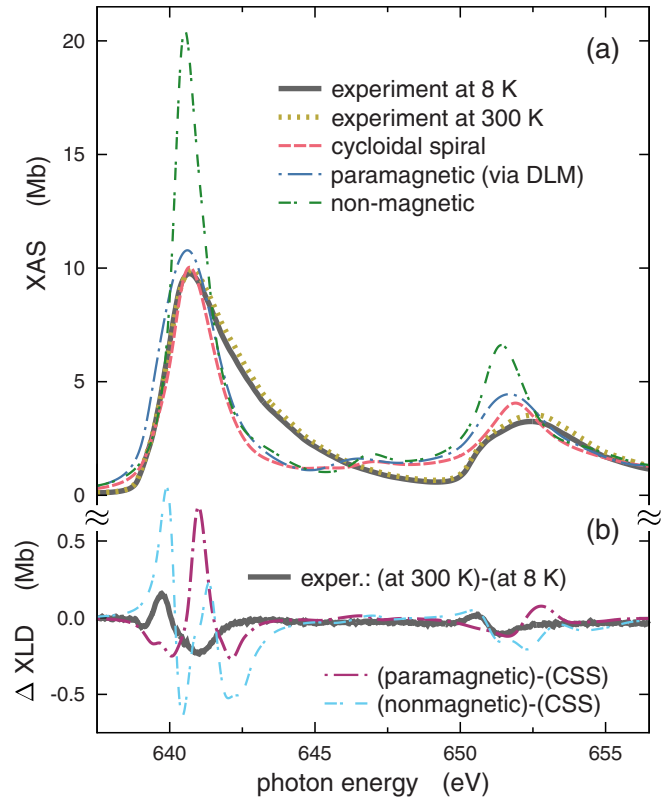

FIG. 4. (a) Experimental XAS recorded at 8 and 300 K together with theoretical XAS calculated for a CSS state, for a paramagnetic state, and for a nonmagnetic state. (b) Difference of experimental XLD signals recorded at 300 and 8 K compared to the differences between respective theoretical XLD signals obtained by assuming a paramagnetic or a nonmagnetic state at 300 K and a CSS state at 8 K.

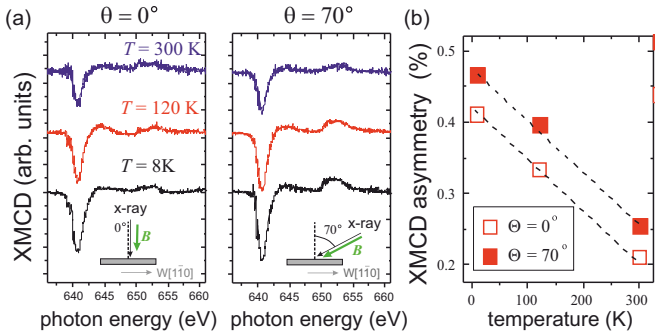

FIG. 5. (a) Experimental Mn $L_{2,3}$-edge XMCD spectra of Mn/W(110) for $T = 8$, 120, and 300 K, for $\Theta = 0^\circ$ (normal incidence) and $\Theta = 70^\circ$ (grazing incidence). An external magnetic field of $B = 5$ T has been applied as indicated in the insets. (b) The temperature dependence of corresponding XMCD asymmetries both for the normal and for the grazing incidence.

magnetic moments survive up to high temperatures whereas the magnetic order has already decayed [34,35].

To isolate the influence of the temperature on XLD, the difference between XLD signals measured for $T = 8$ and 300 K,

$$\mathrm{XLD}(300\ \mathrm{K}) - \mathrm{XLD}(8\ \mathrm{K})$$

is presented in Fig. 4(b). This difference is smaller than but comparable to the intensity of the XLD signals themselves [cf. Fig. 2(b)]. This suggests that changes, indeed, happen in the system if the temperature increases. At the same time, the change in the experimental XLD between $T = 8$ and 300 K is quite different from the change in the theoretical XLD when going from a CSS to a paramagnetic state or from a CSS to a nonmagnetic state (see the respective differences in Fig. 4). We can, thus, infer that at room temperature the system is neither nonmagnetic nor paramagnetic. The exact nature of the temperature-induced changes in the magnetic state of Mn/W(110) remains unknown.

C. Temperature-dependent field-induced XMCD

The XMCD spectra were measured for polar ($\Theta = 0^\circ$, photon beam parallel to W[110]) and grazing ($\Theta = 70^\circ$, photon beam inclined towards the W[1$\bar{1}$0] direction) incidence. To induce nonzero average magnetization in the sample, an external magnetic field of $B = 5$ T was applied along the x-ray's incidence direction. The azimuthal orientation of the tungsten crystal was kept the same as during the XLD measurements, that is, $\phi = 0^\circ$. The measurements were performed for three temperatures ($T = 8$, 120, and 300 K).

The results are summarized in Fig. 5: Fig. 5(a) shows the temperature-dependent field-induced XMCD spectra, Fig. 5(b) presents the respective XMCD asymmetries derived from the peak heights. The XMCD signal is very small: The XMCD asymmetry at the L_3 peak is at most 0.5% (at $\Theta = 70^\circ$ and $T = 8$ K). For comparison, Mn in a ferromagnetic state with $\boldsymbol{M}$ fully aligned along the x-ray direction would exhibit an XMCD asymmetry of about 30% [36]. We stress that the effect we observe is a field-induced (nonremanent) XMCD [37]; we checked that the XMCD signal disappears when the external field is decreased to zero. This is in contrast to common XMCD experiments on ferromagnets where the external magnetic field is used just to orient the magnetic domains and where, therefore, a nonzero XMCD signal remains after the external field has been withdrawn. Absence of a zero-field XMCD signal can, thus, serve as evidence that there are no ferromagnetic regions in the sample. Such a confirmation could not be obtained via more traditional magnetization measurements because the amount of magnetic material is very small in this case.

The XMCD signal is sensitive to the projection of the magnetic moment of the photoabsorbing atom along the direction of the incoming photons. Quantitatively, the XMCD intensity I_{XMCD} scales as

$$I_{\mathrm{XMCD}} \sim \cos\alpha, \tag{6}$$

where α is the angle between the direction of the incoming x rays and the magnetic moment [38]. To get a more specific idea how the measured signal may arise, we calculated the Mn $L_{2,3}$-edge XMCD of Mn/W(110) for a normal incidence photon beam, considering different magnetic configurations to model the effect of the external magnetic field on the arrangement of the magnetic moments. First, we assume that the system is nearly antiferromagnetic with magnetic moments at Mn atoms oriented in plane along the W[1$\bar{1}$0] direction but additionally tilted out of plane by 5° (in the W[110] direction). The second model is a simple ferromagnetic state with a magnetization oriented along W[110] (i.e., out of plane). Finally, we employed an uncompensated DLM model: The magnetic moments are parallel to W[110], but unlike in the paramagnetic case (dealt with in Sec. III B), there is a slight preference in the spin orientation (51% versus 49%). There is no magnetic order in the third model; it could be viewed as a slightly biased set of disordered local moments.

Calculated XAS and XMCD spectra for the theoretical models are shown in Fig. 6 together with experiment. Note that the theoretical XMCD signal was scaled down by a factor of 7 for the tilted AFM model and by a factor of 70 for the ferromagnetic configuration. From comparison of the theoretical XMCD with the experiment it follows that the observed field-induced XMCD is compatible with the model where the antiferromagnetically ordered magnetic moments are tilted a bit in the direction of the external magnetic field. Note, in particular, that the faint shoulder on the low-energy side of the L_3-edge peak (at 639 eV—see the arrow in Fig. 6) is present both in experiment and in theory (see the arrow in Fig. 6).

Interestingly, the ferromagnetic model yields a XMCD signal very similar in shape to the signal for the tilted AFM model—just ten times more intensive. On the other hand, the uncompensated DLM model simulating a magnetically disordered system with a slight prevalence of magnetic moments along the external field is incompatible with the experiment. As the measured XMCD spectral shape does not change significantly between 8 and 300 K [despite the slight changes in intensity—see Fig. 5(a)], the incompatibility of the uncompensated DLM model gives us a strong indication that there is no magnetic phase transition to a paramagnetic state within the temperature range we explored.

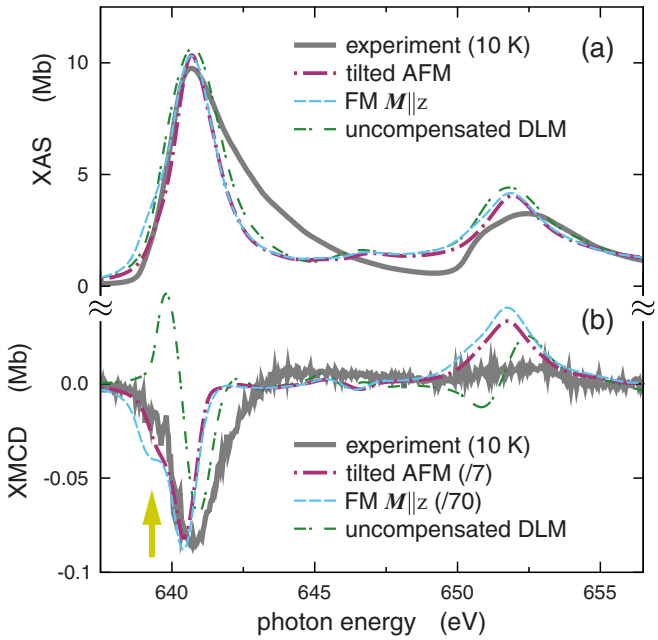

FIG. 6. (a) Experimental XAS and (b) field-induced XMCD recorded at 8 K compared to theoretical spectra calculated for system: (i) in an uncompensated DLM state, (ii) in a ferromagnetic state, and (iii) in an AFM state with moments nearly in plane but tilted by 5° in the out-of-plane direction. Note that the XMCD signal for the tilted AFM state was divided by 7, and the XMCD signal for the ferromagnetic state was divided by 70.

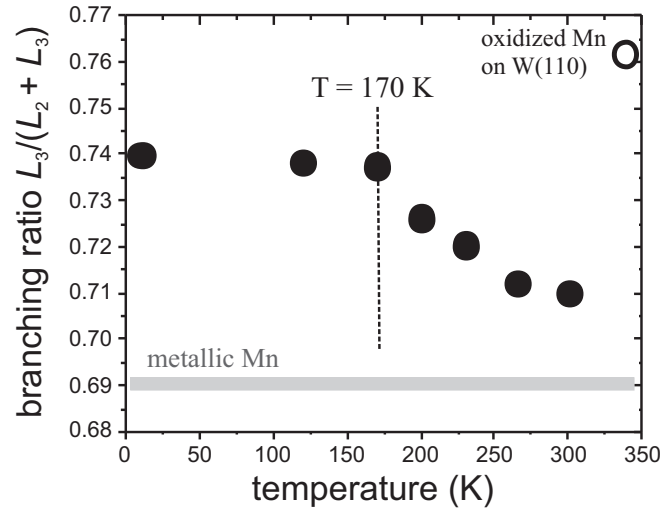

FIG. 7. Experimental branching ratios $I_{L_3}/(I_{L_2} + I_{L_3})$ for Mn $L_{2,3}$-edge XAS spectra at different temperatures.

Considering Fig. 6, it seems that the mechanism how the external magnetic field induces nonzero magnetization in the Mn/W(110) system is via tilting the Mn magnetic moments slightly towards the direction of the external field. Some quantitative assessments can be performed in this respect. By assuming for simplicity that all Mn moments are oriented in the same direction, we can estimate angle α between this direction and the surface normal by means of Eq. (6). Considering the intensity of the calculated Mn L_3-edge XMCD peak for the ferromagnetic model, we get the correct scaling for $\alpha = 89.2°$. The AFM model with moments tilted from the in-plane direction leads to $\alpha = 89.3°$. Obviously, both models are very simple—they disregard the spin spiral nature of the magnetic ground state. Therefore, discrepancies between the measured field-induced XMCD signal and the XMCD calculated for the models have to be expected (cf. Fig. 6). Nevertheless, the good agreement between both estimates of α suggests that the idea that the XMCD spectra are generated through tilting of Mn magnetic moments by the external field is plausible.

This interpretation is consistent with the dependence of the XMCD asymmetry on temperature shown in Fig. 5(b). The decrease in the XMCD asymmetry with increasing temperature results, in this view, from increased thermal disorder and, hence, larger resistance of the spins to be aligned by an external field. The linear decrease in the XMCD intensity with temperature presents another argument in favor of the absence of a magnetic phase transition towards a paramagnetic state within the experimental range of temperatures: For such a phase transition one would expect a clear discontinuity in the susceptibility.

Figure 5(b) moreover reveals that for all temperatures the induced XMCD effect is 20% smaller at polar incidence ($\Theta = 0°$, the external magnetic field is out of plane) compared to that of grazing incidence ($\Theta = 70°$, the external magnetic field is in plane). This anisotropy is consistent with an in-plane easy axis direction along W[1$\bar{1}$0] previously reported experimentally for a Mn monolayer on W(110) and predicted by theory [2]. Namely, one can assume that field-induced alignment of magnetic moments along the hard axis will be less efficient compared to alignment along the easy axis, resulting, thus, in a smaller average projected magnetic moment along the out-of-plane direction.

D. Temperature-dependent XAS branching ratio

The ratio of L_3 and L_2 intensities in nondichroic XAS spectra of transition metals contains information on the d-shell spin state. It can be quantified by the branching ratio (BR) defined as

$$\frac{I_{L_3}}{I_{L_2} + I_{L_3}}, \tag{7}$$

where I_{L_3} and I_{L_2} are integrated intensities of the XAS white lines at the respective edges. We quantified these intensities by subtracting a standard two-step-function background from the measured XAS and integrated the peaks in the energy ranges of 637.5–649.5 and 649.5–670.0 eV to get I_{L_3} and I_{L_2}, respectively.

BRs are shown in Fig. 7 for different temperatures; they were evaluated for Mn $L_{2,3}$-edge spectra recorded for the $\phi = 0°$ azimuthal orientation of the W crystal. For low temperatures the BR is constant (BR = 0.74; $I_{L_3}/I_{L_2} = 2.85$). If the temperature increases above $T = 170$ K, the values drop steadily, and at room temperature BR reaches 0.71, which is closer to that of metallic Mn (BR = 0.69 [32]) and to the statistical value of 2/3. For comparison—the corresponding

values for 14 ML of Mn on fcc Co(001) are BR = 0.72 and $I_{L_3}/I_{L_2} = 2.55$ [39].

According to Thole and van der Laan [40] the BR of 3*d* transition metals reflects the electronic *d*-shell configuration, which determines the local moment per atom. An abrupt change in the *d*-shell configuration clearly occurs when exposing our Mn monolayer samples to oxygen: oxygen contamination leads to a characteristic multiplet structure in the XAS spectral shape corresponding to a Mn^{2+} state (similar to that of MnO shown in Fig. 9). In the oxidized state the BR jumps to higher values of about 0.76 (see data point at $T = 338$ K in Fig. 7), which is consistent with BR's reported for MnO with a d^5 occupancy [41].

The observed small decay of the $I_{L_3}/I_{L_3+L_2}$ branching ratio between 170 and 300 K (disregarding the oxidized case) suggests a subtle but continuous change in the Mn *d*-shell spin configuration with temperature. Interestingly, this happens in the range where the temperature-induced changes in the XLD peaks are small in comparison with the changes for $T \lesssim 170$ K (see Fig. 3). One should bear in mind that the BR does not reflect magnetic order but only the magnitude of the local moments per atom.

IV. DISCUSSION

Mn/W(110) is a system where the XLD would arise even without any magnetism, just because of the nonfourfold symmetry of the bcc (110) surface. However, the magnetic state has a profound influence on the shape of the XLD spectra (see Fig. 2). So in common terminology one could speak about natural dichroism in the presence of magnetization. It is not possible to disentangle the structural and magnetic contributions to XLD from each other. This is because magnetization has a strong influence on the electronic structure as demonstrated by comparing the DOS for magnetic and nonmagnetic Mn/W(110) (Fig. 13 in Appendix E). Forcing Mn to be nonmagnetic would change the spectra substantially, similarly, as if Mn was replaced by a different chemical element.

The XLD spectrum depends on the direction of the magnetic moments. This is crucial for distinguishing between helical and cycloidal spin spirals. The direction of magnetic moments is connected to the Mn/W(110) system via spin-orbit coupling (SOC). The importance of SOC is illustrated in Appendix F where it is shown how XLD changes if the direction of antiferromagnetically coupled magnetic moments at Mn atoms varies. Spin-orbit interaction, thus, always has to be considered when analyzing linear dichroism for magnetic systems, even in cases where an essential part of the dichroism originates from the structure.

The dependence of magnetism of Mn/W(110) on temperature appears to be complicated. We observe signs of a crossover at 170 K: beyond this temperature, the rate of change of XLD spectra with temperature drops (Sec. III B, Fig. 3) and the BR starts to vary (Sec. III D, Fig. 7). On the other hand, the temperature dependence of field-induced XMCD does not exhibit any signs of crossover (Sec. III C, Fig. 5). The changes in XLD or BR at 170 K are visible but not dramatic, and, thus, we do not regard them as signatures of a magnetic phase transition. As concerns the $T = 300$-K case, which is the highest temperature we explored, we have strong indications that there are local magnetic moments at Mn atoms (Sec. III B, Fig. 4) and that these moments are not disordered as in a paramagnetic system (Sec. III B, Fig. 4 and Sec. III C, Fig. 5).

Multiscale calculations of Hasselberg *et al.* [10] do not find any intermediate magnetic state between the CSS ground state and the state without magnetic order. In their calculations the crossover temperature between the ordered and the disorder state was found to be around 510 K [10], which is significantly higher than 240 K deduced from STM experiments [10,11]. Our XAS, XLD, and XMCD measurements do not reveal a magnetic phase transition or a major change of the magnitude of the magnetic moment per atom below 300 K, in agreement with the predictions of Hasselberg *et al.* [10].

It was suggested that the apparent loss of magnetic order seen in STM experiments could be due to thermal depinning of the spin spirals. Depinning effects would not affect our experimental data: XAS yields an almost instantaneous snapshot of the magnetic state of the system, contrary to STM, which yields information averaged over the millisecond timescale necessary to perform typical differential conductance measurements in a lock-in mode. XAS, thus, provides information complementary to the information obtained by STM.

Based on our data, it is difficult to assess the significance of the crossover observed in the temperature dependence of XLD and BR around 170 K. Possibly, an important factor can be that our samples contain Mn monolayer stripes of different widths in the [001] direction and that x-ray absorption spectroscopy probes many of them at the same time. Sessi *et al.* [11] found that magnetic properties of Mn stripes depend on these widths. It is conceivable that different parts of the sample are in a different magnetic state and that this state varies with the temperature depending on the size of the respective Mn island. The measured signal would then be a superposition of different signals. One should also have in mind that XAS will stress the role of large Mn monolayer terraces (in comparison to short terraces) because that is where most of the Mn atoms are sitting. Open questions clearly remain.

V. CONCLUSIONS

X-ray linear dichroism can be used as a probe for noncollinear magnetic order. Cycloidal and helical spin spirals give rise to significantly different Mn $L_{2,3}$-edge XLD signals for Mn/W(110), enabling, thus, to distinguish between these two configurations. The magnetic ground state of Mn/W(110) is an AFM cycloidal spin spiral.

Based on temperature-dependent XAS, XLD, and field-induced XMCD spectra we deduce that the magnetic order of Mn/W(110) varies with temperature, but this variation lacks a clear indication of a phase transition in the investigated range (8–300 K). Local magnetic moments at Mn atoms are present for temperatures up to 300 K.

A crossover exists in the temperature dependence of XAS branching ratios and in XLD profiles around 170 K, but it is not present in XMCD data. The ground-state magnetic order (AFM cycloidal spin spiral) appears to be weakened

and possibly partially disrupted at these temperatures, but the system is not paramagnetic even up to 300 K. Tentatively, the observed trends may result from the fact that x-ray absorption provides an instantaneous view on the magnetic properties averaged over a set of Mn islands with a variety of sizes and shapes: For some Mn islands, the system might be in another—yet undetermined—magnetic state.

ACKNOWLEDGMENTS

This work was supported by the GA ČR via Project No. 20-18725S. Additionally, computing resources were supported by Project No. CEDAMNF CZ.02.1.01/0.0/0.0/15_003/0000358 (Ministry of Education, Youth and Sports) and by Project "e-Infrastruktura CZ" (Project No. e-INFRA LM2018140) provided within the program Projects of Large Research, Development and Innovations Infrastructures. Soft x-ray experiments were carried out at the ESRF facilities (beamline ID08) during Projects No. HE3406 and No. HE3638. We acknowledge financial support (travel, accommodation, and subsistence) by the ESRF for both projects. The evaluation of synchrotron data was supported partly by the Project No. SOLID21 CZ.02.1.01/0.0/0.0/16_019/0000760 of the Ministry of Education, Youth and Sports. Finally, we thank the DFG for financial support via the Cluster of Excellence "Advanced Imaging of Matter" (EXC 2056, Project No. 390715994).

APPENDIX A: STM IMAGES OF THE SUBSTRATE AND THE SAMPLE

Typical STM images of a clean W(110) surface are shown in Figs. 8(a) and 8(c). In the clean state typical carbon-induced (15×3) reconstructions have disappeared in the LEED patterns. STM images demonstrating the step-flow growth of Mn monolayer stripes (referred to in Sec. II A) are presented in Figs. 8(b) and 8(d).

APPENDIX B: INTERNAL CONSISTENCY OF XLD MEASUREMENTS

A typical featureless XLD signal of randomly oriented polycrystalline MnO powder is plotted in the lower graph of Fig. 9 (cf. Ref. [42]). Small shifts in photon energy calibration between measuring the spectra for ϵ_h and ϵ_v photon polarization would produce spurious nonzero XLD signals at the Mn $L_{2,3}$ edges with a characteristic derivative character. We comment here that, indeed, such artifacts appeared when the photon polarization vector was set to angles other than the standard ϵ_h and ϵ_v undulator configurations. Therefore, to study the dependence of XLD on the azimuthal orientation of the sample, we kept the polarization vectors ϵ_h and ϵ_v constant and instead rotated the W(110) crystal.

For a C_{2v} symmetric crystal surface we expect a twofold symmetric dependence of XAS signals versus azimuthal in-plane ϵ orientations in polar incidence geometry ($\Theta = 0°$). The C_{2v} symmetry of the W(110) crystal surface should lead to a fundamental dichroism between the W[100] and the W[1$\bar{1}$0] directions. For a pseudomorphically grown Mn monolayer, the spin texture would obey this symmetry. For a C_{2v} symmetry fundamental XLD spectra should scale as $\cos(2\phi)$, where ϕ is the angle between the W[1$\bar{1}$0] high-symmetry direction and the ϵ_h incoming photon polarization vector [43]: XLD is largest at $\phi = 0°$ and vanishes at $\phi = 45°$. We verified this behavior by measuring XLD for Mn/W(110) in two azimuthal orientations $\phi = 0°$ and 48°. Respective data are shown in Fig. 10(a). Although the average XAS intensity is equivalent for $\phi = 0°$ and 48° (upper graph), the XLD signal at $\phi = 48°$ is reduced and reversed in sign compared to that of $\phi = 0°$. The respective factor is $\cos(2 \times 48°) = -0.105$ [see the lower graph in Fig. 10(a)]. The shape of the XLD, however, is the same within the resolution of the experiment, affirming a strict C_{2v} symmetry of the system. Respective LEED patterns in Fig. 10(b) show the azimuthal rotation of the W(110) crystal by 48°, corresponding to the $\phi = 0°$ and 48° measuring geometries.

APPENDIX C: MODELING SPIN SPIRALS BY AVERAGING OVER AFM CONFIGURATIONS

Spectra for spin spirals are calculated as averages over spectra for two AFM configurations with perpendicular directions of the magnetization. Figure 11 demonstrates that this approach is justified. We calculated the spectra for proper helical and cycloidal spin spirals with a wavelength $\lambda = 7.2$ nm (i.e., 16 interatomic distances between Mn atoms along the W[1$\bar{1}$0] direction in which the spiral propagates). A fully relativistic calculation is needed to account for the effect of SOC, therefore, appropriate supercells have to be involved

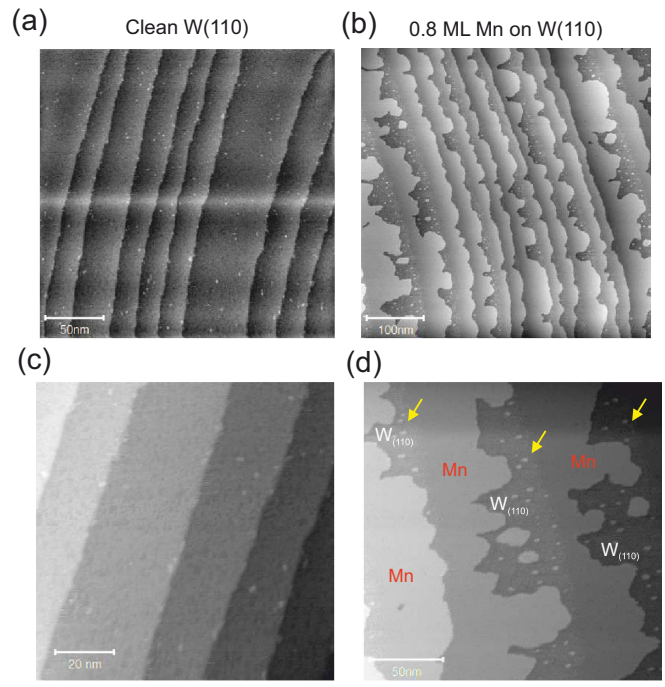

FIG. 8. *In situ* sample characterization in the ID8 preparation chamber by scanning tunneling microscopy. (a) Clean W(110) substrate with multiple terraces. (b) Step-flow growth of monolayer Mn stripes on W(110) at Mn coverages of about 0.8 MLs. (b) and (d) show images of respective sample areas on a smaller scale. Tungsten step edges are indicated by yellow arrows.

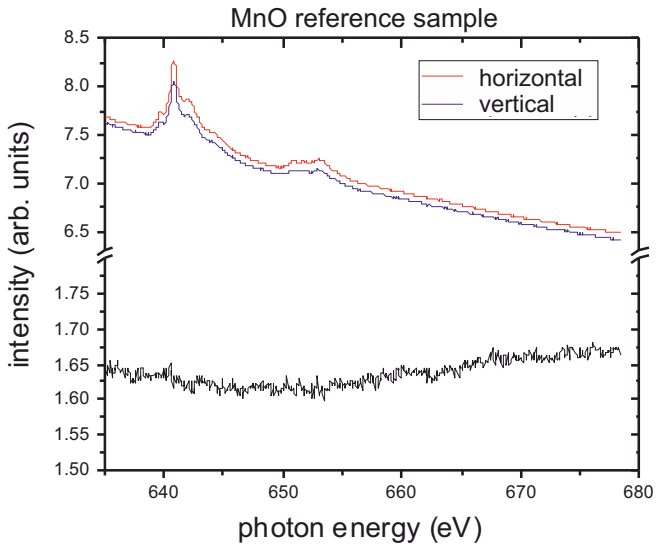

FIG. 9. XAS and XLD signals measured for the polycrystalline MnO reference sample. Top graph: XAS for horizontal and vertical photon polarizations ϵ_h and ϵ_v. Bottom graph: XLD signal resulting from the XAS spectra shown above. The constant offset of XLD values reflects the offset in the raw data in the top graph as they are not normalized to 1 at 637 eV.

(the generalized Bloch theorem simplifying the calculations for spin spirals [44,45] cannot be used if SOC is present). This makes the computation very demanding, so we resorted to the atomic sphere approximation (ASA) for the potential and neglected the core hole in this test. The Mn $L_{2,3}$-edge XLD for a helical spin spiral is compared to the average of XLD spectra for AFM configurations with $\boldsymbol{M} \parallel$ W[001] and with $\boldsymbol{M} \parallel$ W[110] in Fig. 11(a). The Mn $L_{2,3}$-edge XLD for a cycloidal spin spiral is compared to the average of XLD spectra for AFM configurations with $\boldsymbol{M} \parallel$ W[1$\bar{1}$0] and with $\boldsymbol{M} \parallel$ W[110] in Fig. 11(b). There is nearly a perfect match between the results obtained by both approaches. We checked that the same conclusions can be reached also if the average is made not only just of two, but also of three or five AFM configurations with different magnetization directions.

Our approach effectively neglects the angle between adjacent spin directions, so it is the better the longer the spiral wavelength is. The wavelength of the spin spirals observed experimentally for Mn/W(110) is 12 nm [5,46], which is even longer than the wavelength used in our test calculation. Modeling spectra of spin spirals by averages over spectra of two collinear AFM configurations with perpendicular directions of the magnetization is, thus, justified in our case.

APPENDIX D: INFLUENCE OF THE CORE HOLE ON THE CALCULATED SPECTRA

In metals, the presence of the core hole is usually not the decisive factor for the shape of XAS spectra (even though accounting for it often improves the agreement between theory and experiment). However, we deal with XLD and its variations, which is quite a subtle effect demanding a high accuracy. We present in Fig. 12 Mn $L_{2,3}$-edge XAS and XLD spectra for a CSS magnetic configuration calculated if the

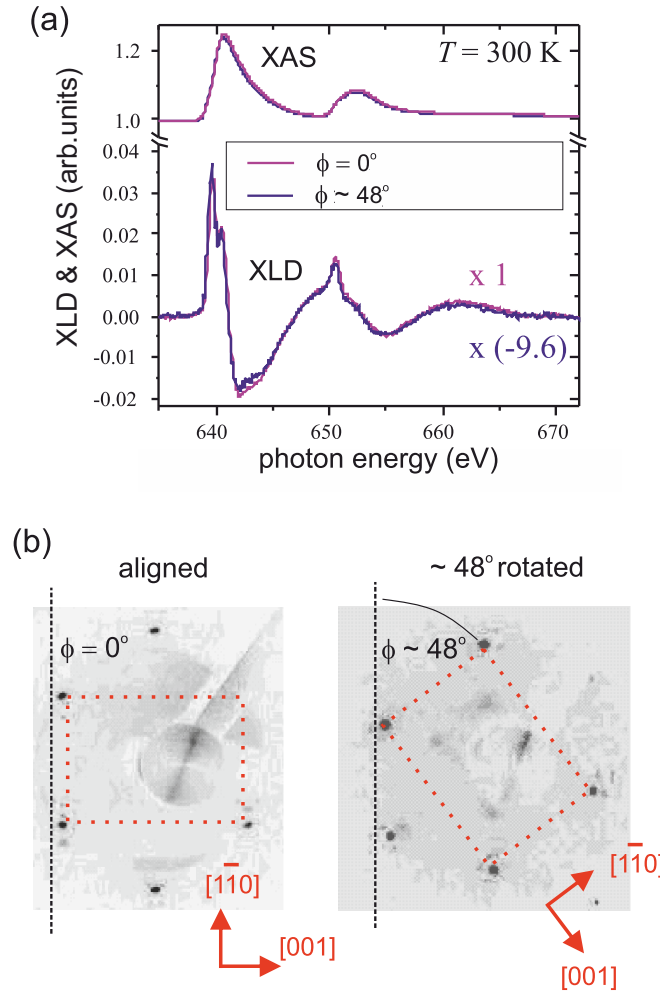

FIG. 10. Scaling of the Mn $L_{2,3}$-edge XLD intensity under azimuthal rotation of the W(110) substrate. All data were measured at $T = 300$ K. (a) Mn $L_{2,3}$-edge XAS and XLD for angles $\phi = 0°$ and 48° between the W[1$\bar{1}$0] direction and the ϵ_h photon polarization vector. XLD data for $\phi = 48°$ are shown multiplied by $1/\cos(2\phi)$. (b) LEED images used for deducing the azimuthal orientation of the crystal.

core hole is ignored (i.e., for a ground-state potential), if the core hole is included via the final-state approximation, and if the Slater transition state method is used (as the final-state approximation but with only half of the core hole). A detailed description of the procedures can be found in Ref. [27]. The presence of the core hole does not alter the XAS spectrum substantially (similar to metallic Fe or Co [30]), however, it makes a significant difference for the XLD spectra. On the other hand, there is no big difference between the effect of a full core hole and of a half core hole (Slater transition state). This indicates some robustness in our treatment of the core hole.

APPENDIX E: INFLUENCE OF MAGNETISM ON DOS

To highlight the differences between the case with magnetic and with nonmagnetic Mn atoms, we present in Fig. 13 the DOS at Mn atoms for Mn/W(110) if the system is

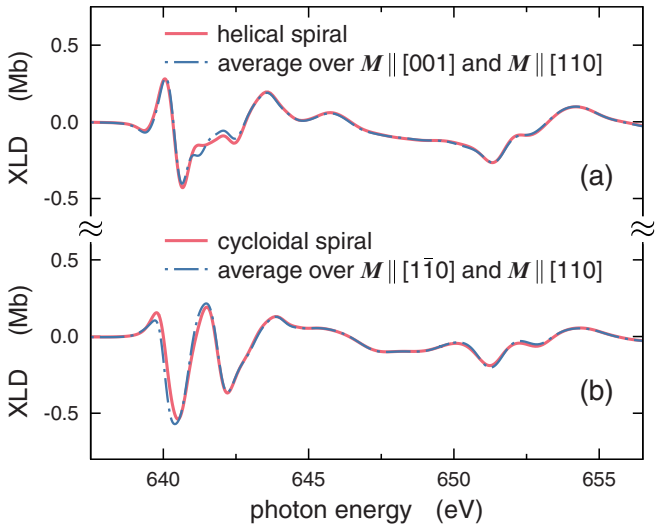

FIG. 11. Theoretical Mn $L_{2,3}$-edge XLD spectra for spin spirals compared to averages of spectra for AFM configurations for two perpendicular magnetization directions. Calculations performed within the ASA without a core hole.

nonmagnetic and if it is in an AFM state. One can see that the DOS is totally different for these two cases, similar to what would happen if Mn was replaced by another element. This means, among others, that it is not possible to separate the structural contribution to XLD from the magnetic contribution by calculating XLD for Mn/W(110) with nonmagnetic Mn: One would deal with a totally different system in each case.

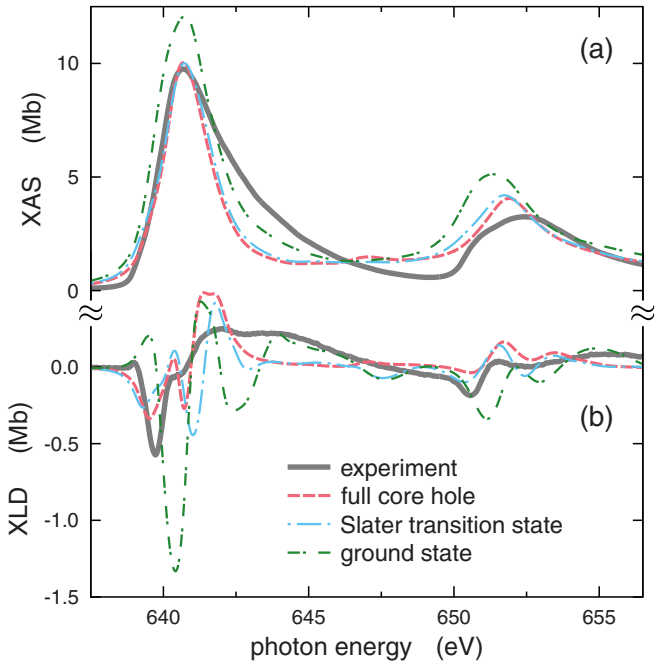

FIG. 12. Mn $L_{2,3}$-edge XAS and XLD calculated for the ground-state potential (core hole ignored), for the potential corresponding to the Slater transition state (half core hole) and for the potential obtained by means of the final-state approximation (full core hole). The experimental spectrum is shown for comparison.

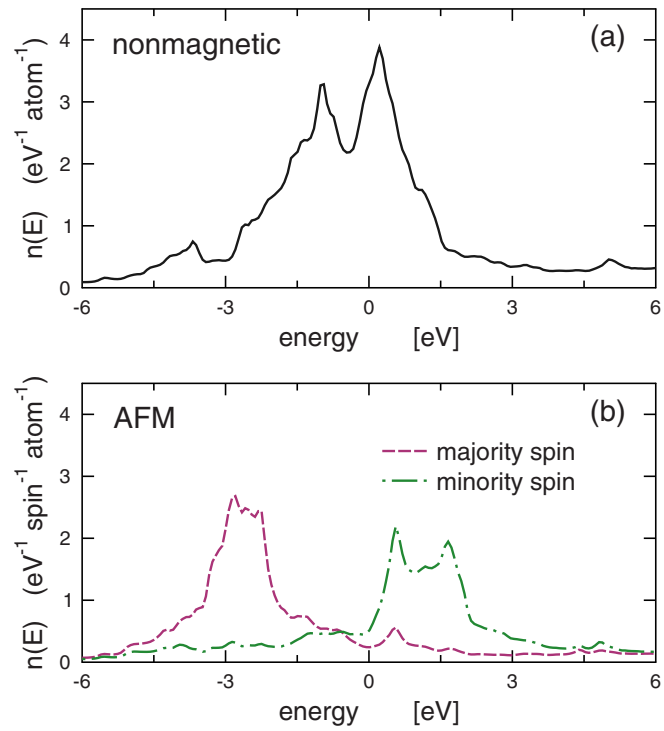

FIG. 13. DOS at Mn atoms calculated for (a) nonmagnetic and (b) AFM configurations of Mn/W(110). The spin channels are shown separately for the AFM state and summed together for the nonmagnetic state.

APPENDIX F: INFLUENCE OF SOC ON XLD

SOC is an important factor affecting XLD of magnetic systems. Figure 14 shows Mn $L_{2,3}$-edge XLD spectra for Mn/W(110) calculated for collinear AFM configurations, assuming that the direction of the magnetic moments is parallel to one of three mutually perpendicular directions: W[001], W[1$\bar{1}$0], and W[110] (see Fig. 1 for a visual idea of these

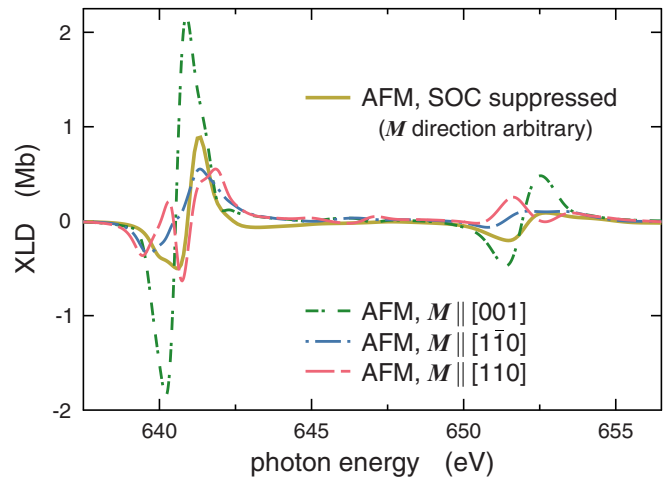

FIG. 14. Mn $L_{2,3}$-edge XLD for Mn/W(110) in an AFM state with the direction of magnetic moments $\boldsymbol{M}$ oriented along W[001], W[1$\bar{1}$0], and W[110]. A XLD spectrum calculated with SOC suppressed is shown for comparison.

directions). One can see that the direction of the magnetic moments (linked to the structure via SOC) has a significant impact.

It would be instructive to compare these data with results obtained without the SOC. This is conceptually questionable because suppressing SOC completely (as in the scalar-relativistic formalism) would remove the difference between the L_2 and the L_3 edges altogether. To suppress the SOC whereas keeping the distinction between L_2 and L_3 spectra we adopt a mixed approach: (i) We suppress the SOC for the valence states, using an approximate two-component scheme [47] employed earlier, e.g., for studying the magnetocrystalline anisotropy [48], and (ii) we suppress the relativistic exchange splitting of the $2p$-core levels pertaining to the same relativistic quantum number κ (see, e.g., Ref. [49] for decomposition of the L_3- and L_2-white lines into relevant components). This second step is analogous to the model of Kuneš and Oppeneer [19]. The Mn $L_{2,3}$-edge XLD spectrum calculated in this way is labeled as "SOC suppressed" in Fig. 14. It does not depend on the direction of the magnetic moments and can be seen as the outcome of a nonrelativistic calculation.

It is evident that relativistic (SOC-related) effects are crucial.

[1] M. Bode, S. Heinze, A. Kubetzka, O. Pietzsch, X. Nie, G. Bihlmayer, S. Blügel, and R. Wiesendanger, Phys. Rev. Lett. **89**, 237205 (2002).

[2] M. Bode, S. Heinze, A. Kubetzka, O. Pietzsch, M. Hennefarth, M. Getzlaff, R. Wiesendanger, X. Nie, G. Bihlmayer, and S. Blügel, Phys. Rev. B **66**, 014425 (2002).

[3] S. Heinze, M. Bode, A. Kubetzka, O. Pietzsch, X. Nie, S. Blügel, and R. Wiesendanger, Science **288**, 1805 (2000).

[4] S. Dennler and J. Hafner, Phys. Rev. B **72**, 214413 (2005).

[5] M. Bode, M. Heide, K. von Bergmann, P. Ferriani, S. Heinze, G. Bihlmayer, A. Kubetzka, O. Pietzsch, S. Blügel, and R. Wiesendanger, Nature (London) **447**, 190 (2007).

[6] M. Haze, Y. Yoshida, and Y. Hasegawa, Sci. Rep. **7**, 13269 (2017).

[7] D. Serrate, Y. Yoshida, M. Moro-Lagares, A. Kubetzka, and R. Wiesendanger, Phys. Rev. B **93**, 125424 (2016).

[8] S. Haldar and S. Heinze, Phys. Rev. B **98**, 220401(R) (2018).

[9] M. Gutzeit, S. Haldar, and S. Heinze, Phys. Rev. B **101**, 134411 (2020).

[10] G. Hasselberg, R. Yanes, D. Hinzke, P. Sessi, M. Bode, L. Szunyogh, and U. Nowak, Phys. Rev. B **91**, 064402 (2015).

[11] P. Sessi, N. P. Guisinger, J. R. Guest, and M. Bode, Phys. Rev. Lett. **103**, 167201 (2009).

[12] M. Menzel, Y. Mokrousov, R. Wieser, J. E. Bickel, E. Vedmedenko, S. Blügel, S. Heinze, K. von Bergmann, A. Kubetzka, and R. Wiesendanger, Phys. Rev. Lett. **108**, 197204 (2012).

[13] W. Kuch, L. I. Chelaru, F. Offi, J. Wang, M. Kotsugi, and J. Kirschner, Phys. Rev. Lett. **92**, 017201 (2004).

[14] C. Grazioli, D. Alfè, S. R. Krishnakumar, S. S. Gupta, M. Veronese, S. Turchini, N. Bonini, A. Dal Corso, D. D. Sarma, S. Baroni, and C. Carbone, Phys. Rev. Lett. **95**, 117201 (2005).

[15] C. Luo, H. Ryll, C. H. Back, and F. Radu, Sci. Rep. **9**, 18169 (2019).

[16] F. Nolting, A. Scholl, J. Stohr, J. W. Seo, J. Fompeyrine, H. Siegwart, J.-P. Locquet, S. Anders, J. Lüning, E. E. Fullerton, M. F. Toney, M. R. Scheinfein, and H. A. Padmore, Nature (London) **405**, 767 (2000).

[17] E. Arenholz, G. van der Laan, R. V. Chopdekar, and Y. Suzuki, Phys. Rev. B **74**, 094407 (2006).

[18] P. Wadley, V. Hills, M. R. Shahedkhah, K. W. Edmonds, R. P. Campion, V. Novák, B. Ouladdiaf, D. Khalyavin, S. Langridge, V. Saidl, P. Nemec, A. W. Rushforth, B. L. Gallagher, S. S. Dhesi, F. Maccherozzi, J. Železný, and T. Jungwirth, Sci. Rep. **5**, 17079 (2015).

[19] J. Kuneš and P. M. Oppeneer, Phys. Rev. B **67**, 024431 (2003).

[20] J. P. Perdew, K. Burke, and M. Ernzerhof, Phys. Rev. Lett. **77**, 3865 (1996).

[21] H. Ebert, D. Ködderitzsch, and J. Minár, Rep. Prog. Phys. **74**, 096501 (2011).

[22] H. Ebert, The SPRKKR package version 8, https://www.ebert.cup.uni-muenchen.de (2019)

[23] R. Zeller, P. H. Dederichs, B. Újfalussy, L. Szunyogh, and P. Weinberger, Phys. Rev. B **52**, 8807 (1995).

[24] N. Hauptmann, S. Haldar, T.-C. Hung, W. Jolie, M. Gutzeit, D. Wegner, S. Heinze, and A. A. Khajetoorians, Nat. Commun. **11**, 1197 (2020).

[25] R. Zeller, J. Phys. C: Solid State Phys. **20**, 2347 (1987).

[26] T. Huhne, C. Zecha, H. Ebert, P. H. Dederichs, and R. Zeller, Phys. Rev. B **58**, 10236 (1998).

[27] O. Šipr, W. Khan, Y. Joly, and J. Minár, J. Synchrotron Radiat. **26**, 152 (2019).

[28] J. Staunton, B. Gyorffy, A. J. Pindor, G. M. Stocks, and H. Winter, J. Magn. Magn. Mater. **45**, 15 (1984).

[29] H. Suzuki, K. Zhao, G. Shibata, Y. Takahashi, S. Sakamoto, K. Yoshimatsu, B. J. Chen, H. Kumigashira, F.-H. Chang, H.-J. Lin, D. J. Huang, C. T. Chen, B. Gu, S. Maekawa, Y. J. Uemura, C. Q. Jin, and A. Fujimori, Phys. Rev. B **91**, 140401(R) (2015).

[30] O. Šipr, J. Minár, A. Scherz, H. Wende, and H. Ebert, Phys. Rev. B **84**, 115102 (2011).

[31] J.-S. Kang, G. Kim, H. J. Lee, D. H. Kim, H. S. Kim, J. H. Shim, S. Lee, H. Lee, J.-Y. Kim, B. H. Kim, and B. I. Min, Phys. Rev. B **77**, 035121 (2008).

[32] P. Schieffer, C. Krembel, M.-C. Hanf, M.-H. Tuilier, P. Wetzel, G. Gewinner, and K. Hricovini, Eur. Phys. J. B **8**, 165 (1999).

[33] O. Šipr and H. Ebert, Phys. Rev. B **72**, 134406 (2005).

[34] S. S. A. Razee, J. B. Staunton, L. Szunyogh, and B. L. Györffy, Phys. Rev. B **66**, 094415 (2002).

[35] M. Pickel, A. B. Schmidt, M. Weinelt, and M. Donath, Phys. Rev. Lett. **104**, 237204 (2010).

[36] A. P. Holm, S. M. Kauzlarich, S. A. Morton, G. D. Waddill, W. E. Pickett, and J. G. Tobin, J. Am. Chem. Soc. **124**, 9894 (2002).

[37] S. Mankovsky and H. Ebert, Phys. Rev. B **69**, 014414 (2004).

[38] J. Stöhr and H. C. Siegmann, *Magnetism: From Fundamentals to Nanoscale Dynamics* (Springer, Berlin, 2006).
[39] W. L. O'Brien and B. P. Tonner, Phys. Rev. B **50**, 2963 (1994).
[40] B. T. Thole and G. van der Laan, Phys. Rev. B **38**, 3158 (1988).
[41] H. Jung, S.-J. Lee, M. Song, S. Lee, H. J. Lee, D. H. Kim, J.-S. Kang, C. L. Zhang, and S.-W. Cheong, New J. Phys. **11**, 043008 (2009).
[42] B. Gilbert, B. H. Frazer, A. Belz, P. G. Conrad, K. H. Nealson, D. Haskel, J. C. Lang, G. Srajer, and G. De Stasio, J. Phys. Chem. A **107**, 2839 (2003).
[43] G. van der Laan, N. D. Telling, A. Potenza, S. S. Dhesi, and E. Arenholz, Phys. Rev. B **83**, 064409 (2011).
[44] L. M. Sandratskii, J. Phys.: Condens. Matter **3**, 8565 (1991).
[45] S. Mankovsky, G. H. Fecher, and H. Ebert, Phys. Rev. B **83**, 144401 (2011).
[46] M. Haze, Y. Yoshida, and Y. Hasegawa, Phys. Rev. B **95**, 060415(R) (2017).
[47] H. Ebert, H. Freyer, A. Vernes, and G.-Y. Guo, Phys. Rev. B **53**, 7721 (1996).
[48] O. Šipr, S. Mankovsky, S. Polesya, S. Bornemann, J. Minár, and H. Ebert, Phys. Rev. B **93**, 174409 (2016).
[49] O. Šipr, J. Vackář, and J. Minár, J. Synchrotron Radiat. **25**, 523 (2018).